Semirelativistic antisymmetrized molecular dynamics for the production of energetic neutrons in intermediate-energy heavy-ion reactions

Q. Hu [1,2,*] G. Y. Tian [1] R. Wada [3,†] X. Q. Liu [4] W. P. Lin [4] H. Zheng [5] Y. P. Zhang [1,2] Z. Q. Chen [1] R. Han [1] and M. R. Huang [6]

[1]*Institute of Modern Physics, Chinese Academy of Sciences, Lanzhou 730000, China*
[2]*School of Nuclear Sciences and Technology, University of Chinese Academy of Sciences, Beijing 100049, China*
[3]*Cyclotron Institute, Texas A&M University, College Station, Texas 77843, USA*
[4]*Key Laboratory of Radiation Physics and Technology of the Ministry of Education, Institute of Nuclear Science and Technology, Sichuan University, Chengdu 610064, China*
[5]*School of Physics and Information Technology, Shaanxi Normal University, Xi'an 710119, China*
[6]*College of Physics and Electronics information, Inner Mongolia University for Nationalities, Tongliao 028000, China*

(Received 1 July 2023; revised 6 September 2023; accepted 11 October 2023; published 28 November 2023)

Relativistic corrections have been made in the nonrelativistic antisymmetrized molecular dynamics (AMD) simulations to apply to the high-energy neutron production in the $^{12}C+^{12}C$ and $^{16}O+^{12}C$ collisions at incident energies of 290 and 400 MeV/nucleon. The corrections are made in kinematics alone and neither nucleon-nucleon inelastic scatterings nor meson productions are taken into account, and AMD with the relativistic corrections is called semirelativistic AMD. The three-nucleon collision (3*N*C) and Fermi boost in the collision processes are taken into account in the nonrelativistic AMD. Since the relativistic corrections tend to compensate in each other, the difference between the semirelativistic and nonrelativistic results become small. High-energy tails of the available experimental neutron double-differential cross sections, especially at larger angles, are well reproduced by AMD with the 3*N*C term both with nonrelativistic and semirelativistic simulations. These results indicate that the high-energy neutrons are dominantly produced by the 3*N*C process in this incident energy range.

DOI: 10.1103/PhysRevC.108.054907

I. INTRODUCTION

Intermediate heavy-ion collisions in the energy range of tens of MeV to a few GeV/nucleon, evolving rapidly from pre-equilibrium stages of compression and expansion to the deexcitation phase, allow us to investigate nonequilibrium dynamics of finite-size fermion systems as well as the nature of dense and hot nuclear systems [1,2]. The production of subthreshold mesons, high-energy photons and nucleons, which occurs mainly at the beginning of the reaction, can offer information on the nuclear dynamics at the pre-equilibrium stages [2–4]. One of them is the three-nucleon interaction.

The three-nucleon interaction consists of two parts, an attractive part and a repulsive part [5]. The attractive part is typically expressed by two-pion exchange with excitation of an intermediate Δ resonance following the Fujita-Miyazawa diagram [6] and is important at normal and subnormal densities. The repulsive part of the three nucleon process becomes important in heavy-ion reactions at intermediate energies above 100 MeV/nucleon. However, in most of transport models, only the two-body interaction and binary collision term have been implemented. An attempt was made by Bonasera *et al.* in Ref. [7] to extend a Boltzmann-Nordheim-Vlasov (BNV) to include the three nucleon process in a three-nucleon collision (3*N*C) term, since the three-body potential part can be included in the momentum-dependent effective interaction [8]. In the model, the 3*N* collisions can occur when three particles are found inside the same interaction sphere, which is given by the 3*N*C cross section. In Ref. [9], one of the present authors followed this scenario but used the antisymmetrized molecular dynamics (AMD) framework and was able to reproduce rather well the high-energy proton spectra from the BEVALAC experiments at the incident energy up to 137 MeV/nucleon.

On the experimental side, the energy spectra of fast protons from Ar + Ta collisions at 94 MeV/nucleon were measured with the 4π BaF_2 detector array MEDEA [10] at GANIL, France in the 1990s, stimulated by the experimental reports of the surprisingly large cross section for the subthreshold kaon production in Refs. [11–13]. Although the extracted subthreshold kaon production cross sections were far below the values reported earlier, the high-energy proton production studies were extended to other reaction systems, using ^{36,40}Ar, ^{58}Ni, and ^{132}Xe beams on ^{51}V, ^{58}Ni, ^{98}Mo, Ta, and Au targets [14–17]. In these studies, it was found that the protons with the energy three to four times larger than the beam energy per nucleon were observed over a broad angular range. The measured energetic proton spectra and angular distributions were extended well above the kinematic limit, but their results were unable to be reproduced with standard BNV calculations

*qianghu@impcas.ac.cn
†wada@comp.tamu.edu

[14]. However, when they added a 3*N*C contribution based on a perturbed method of the BNV calculations with a sharp cutoff of the Fermi momentum in the initial nuclei, they were able to reproduce the energetic protons reasonably well [14].

For the higher incident energies, two experimental data sets are available for the high-energy nucleon studies. The experiments were carried out for different beam species on different targets at 290–600 MeV/nucleon at the Heavy-Ion Medical Accelerator (HIMAC) facility at the National Institute of Radiological Sciences (NIRS) in Japan, to provide the precise neutron production cross sections in the neutron-energy range of 1 MeV to several hundreds of MeV for cancer therapy [18,19]. It is quite interesting to apply the above models to high-energy neutron productions, since the density of the overlap zone between the projectile and target becomes higher at an early stage of collisions, which enhances the 3*N*C process, and pion production may start to impact the dynamical process. However, the dynamics in the available AMD code is performed in nonrelativistic form and the relativistic treatment may become crucial at the incident energy above 100 MeV/nucleon. We treat the relativistic effects as the corrections to the nonrelativistic AMD calculations for $^{12}C+^{12}C$ and $^{16}O+^{12}C$ at 290 and 400 MeV/nucleon to study the high-energy neutron production. The results of AMD with the relativistic corrections as well as the nonrelativistic AMD are compared with the experimental data.

This paper is organized as follows: The modified AMD models are briefly described in Sec. II. Detail comparisons of high-energy neutron spectra and angular distributions are carried out in Sec. III. A summary is given in Sec. IV.

II. MODIFIED ANTISYMMETRIZED MOLECULAR DYNAMICS MODEL

A. Antisymmetrized molecular dynamics

In the antisymmetrized molecular dynamics (AMD) model, the wave function for an A-nucleon system is described by a Slater determinant $|\Phi\rangle$,

$$|\Phi\rangle = \frac{1}{\sqrt{A!}} \det\left[\varphi_i(j)\right], \tag{1}$$

where $\varphi_i = \phi_{Z_i}\chi_{a_i}$. The spin-isospin state χ_{a_i} of each single-particle state takes $p\uparrow$, $p\downarrow$, $n\uparrow$, and $n\downarrow$. The spatial wave functions of nucleons ϕ_{Z_i} are given by a Gaussian wave function,

$$\langle \mathbf{r}|\phi_{\mathbf{Z_i}}\rangle = \left(\frac{2\nu}{\pi}\right)^{3/4} \exp\left[-\nu\left(\mathbf{r}-\frac{\mathbf{Z}_i}{\sqrt{\nu}}\right)^2 + \frac{1}{2}\mathbf{Z}_i^2\right], \tag{2}$$

where the width parameter $\nu = 0.16$ fm^{-2} [20] is a constant parameter common to all the wave packets. Thus the complex variables $Z \equiv \{\mathbf{Z}_i; i = 1,\ldots,A\} = \{Z_{i\sigma}; i = 1,\ldots,A; \sigma = x,y,z\}$ represent the centroids of the wave packets.

The time evolution of the wave-packet parameters Z is determined by the time-dependent variational principle and the two-nucleon collision process. The former is described as

$$\delta \int dt \frac{\langle\Phi(Z)|\left(i\hbar\frac{d}{dt} - H\right)|\Phi(Z)\rangle}{\langle\Phi(Z)|\Phi(Z)\rangle} = 0. \tag{3}$$

The equation of motion for Z derived from the time-dependent variational principle is

$$i\hbar \sum_{j\tau} C_{i\sigma,j\tau}\frac{dZ_{j\tau}}{dt} = \frac{\partial \mathcal{H}}{Z^*_{i\sigma}}. \tag{4}$$

The matrix $C_{i\sigma,j\tau}$ ($i,j = 1,2,\ldots,A$ and $\sigma,\tau = x,y,z$) is a Hermitian matrix defined by

$$C_{i\sigma,j\tau} = \frac{\partial^2}{\partial Z^*_{i\sigma}\partial Z_{j\tau}} \ln\langle\Phi(Z)|\Phi(Z)\rangle, \tag{5}$$

and $\mathcal{H}$ is the expectation value of the Hamiltonian after the subtraction of the spurious kinetic energy of the zero-point oscillation of the center of mass (CM) of fragments [20],

$$\mathcal{H}(Z) = \frac{\langle\Phi(Z)|H|\Phi(Z)\rangle}{\langle\Phi(Z)|\Phi(Z)\rangle} - \frac{3\hbar^2\nu}{2M}A + T_0[A - N_F(Z)], \tag{6}$$

where $N_F(Z)$ is the fragment number, T_0 is $3\hbar^2\nu/2M$ in principle but treated as a free parameter for an overall adjustment of the binding energies. The Hamiltonian in AMD is given in a nonrelativistic form as

$$H = \sum_{i=1}^{A}\frac{\mathbf{p}_i^2}{2M} + \sum_{i<j} v_{ij}, \tag{7}$$

where M is the nucleon mass and v_{ij} is the potential energy between particle i and particle j. In the present application, the standard Gogny force [21] is used as the effective interaction.

The nucleon-nucleon (NN) collision process is treated as a stochastic process using the above physical coordinates at each time step. The NN collision rate is determined by a given NN cross section under the Pauli principle. The NN cross section is given by

$$\sigma(E,\rho) = \min\left(\sigma_{LM}(E,\rho), \frac{100\text{ mb}}{1 + E/(200\text{ MeV})}\right), \tag{8}$$

where $\sigma_{LM}(E,\rho)$ is the cross section given by Li and Machleidt [22,23]. The angular distribution of proton-neutron scattering are parametrized as

$$\frac{d\sigma_{pn}}{d\Omega} \propto 10^{-\alpha(\pi/2-|\theta-\pi/2|)}, \tag{9}$$

$$\alpha = \frac{2}{\pi}\max\left(0.333\ln E[\text{MeV}] - 1, 0\right), \tag{10}$$

while the proton-proton and neutron-neutron scatterings are assumed to be isotropic.

For cluster production studies, a version of AMD is made in which cluster formation is treated as the final states of the two-body collision process. The version is called AMD-CLUSTER and is described in detail in Ref. [24]. An application of this version for the experimental data for the $^{12}C+^{12}C$ reaction at 50 MeV/nucleon was made and the results were presented in one of our previous publications [25].

B. Fermi boost and 3*N*C process

The stochastic collision process described in the previous section is performed using the centroid of the Gaussian wave packet. Thus the Fermi motion is only taken into account as an average energy and no explicit Fermi motion is taken into account in the collision process. In our previous works as presented in Refs. [9,26], the inclusion of the Fermi-momentum fluctuation in the collision processes and the 3*N*C process were studied for the energetic proton production at the incident energies from 44 to 137 MeV/nucleon, based on the modified versions of the AMD model described in the previous section.

To take into account the Fermi motion explicitly in the dynamical evolution, two stochastic processes are incorporated in the original AMD formulation, which introduces fluctuations in the reaction. One is for the fluctuation during the time evolution of the wave packets in a given effective interaction [27] and the other is the momentum fluctuation added in the collision process [26]. These two stochastic processes made significant improvements to reproduce the experimental data up to the incident energies below 50 MeV/nucleon, as presented in Refs. [26–28].

The former process is an extension of the study of the particle emission from the excited nucleus. Since the equations of motion solved using the centroids of the Gaussian wave packets, the particles emission from an excited nucleus reveals the classical nature; that is, the emission probability increases linearly as the excitation energy increases. When a momentum fluctuation is added in each time step, which is evaluated from the distribution of the Gaussian wave packet, interpreting the distribution as the probability distribution of the momentum of each nucleon, the quantum nature of the particle emission is restored [29]. The quantum diffusion process is an extension of the momentum fluctuation, which is added in phase space according to the Vlasov equation to minimize the deviation of the energy conservation. This modified AMD code was made by Ono *et al.*, and called AMD/D [27].

The above treatment is mainly related to the time evolution of the wave-packet diffusion process and significantly affects on the multifragmentation process but contributes little for the high-energy nucleon emissions. An additional momentum fluctuation, therefore, is added in the collision process to reproduce the high-energy component of the experimental proton energy spectra at the incident energy up to 50 MeV/nucleon in Ref. [26]. The process is called Fermi boost and this version of AMD is called AMD/D-FM. In the actual calculation for given coordinate vectors $\mathbf{r}_1$ and $\mathbf{r}_2$ of two attempt colliding nucleons, the associated momenta $\mathbf{P}_1$ and $\mathbf{P}_2$ are given similarly to Ref. [26] as

$$\mathbf{P}_i = \mathbf{P}_i^0 + \Delta\mathbf{P}_i' \ (i = 1, 2). \tag{11}$$

$\mathbf{P}_i^0$ is the centroid of the Gaussian momentum distribution for the particle i. The second term $\Delta\mathbf{P}_i'$ is the Fermi momentum randomly given along the Gaussian distribution. Since the momentum distribution is partially taken into account in the wave-packet propagation through the diffusion process, the following form of $\Delta\mathbf{P}_i'$ is taken:

$$\Delta\mathbf{P}_i' = \frac{|\Delta\mathbf{P}_i| - cP_{PF}}{|\Delta\mathbf{P}_i|}\Delta\mathbf{P}_i \ (|\Delta\mathbf{P}_i| > cP_{PF})$$
$$= 0 \ (|\Delta\mathbf{P}_i| \leqslant cP_{PF}). \tag{12}$$

cP_{PF} is a correction term to avoid double counting with the diffusion process. At the incident energy above 290 MeV/nucleon, the choice of the c factor is not very sensitive and $c = 0.3$ is used in the present calculation. P_{PF} is a Fermi momentum and $P_{PF} = 250$ MeV/c is taken:

$$\Delta P_{i\tau} = \hbar\sqrt{\nu}(\rho_i/\rho_0)^{1/3}G(1). \tag{13}$$

$G(1)$ is a random number generated along the Gaussian distribution with $\sigma = 1$. $(\rho_i/\rho_0)^{1/3}$ in Eq. (13) is used for taking into account the density dependence empirically. ρ_i is the density at $\mathbf{r}_i$ and ρ_0 is the normal nuclear density. The index τ corresponds to the x, y, z coordinates.

When these models were applied to the experimental data around the incident energies of 100 MeV/nucleon, however, significant deviations were observed between the available experimental proton energy spectra and those of the simulations, as presented in Ref. [9]. To reproduce the experimental data, a 3*N*C process is incorporated in AMD/D-FM, following the work of Bonasera *et al.* in the extended BNV [7]. The Fermi boost is added for the three nucleons when all three pairs of nucleons are within a collision distance, which is evaluated with a constant nucleon-nucleon (NN) cross section of 40 mb. The 3*N*C process is performed in a similar manner to the NN collisions in AMD, following Bonasera's formulation in Ref. [30], and the 3*N*C process is performed along the diagram shown in Fig. 1 [7].

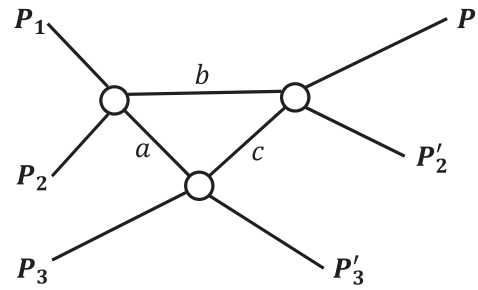

FIG. 1. Diagrammatic representation of 3*N* collision. The lines indicate particle trajectories and the meeting points indicate the location of the particles at the time of collision. $\mathbf{P}_1$, $\mathbf{P}_2$, $\mathbf{P}_3$ represent the initial states and $\mathbf{P}_1'$, $\mathbf{P}_2'$, $\mathbf{P}_3'$, are the final states. a, b, c are intermediate states treated as virtual states in the 3*N* collision process.

In the diagram the 3*N*C process is described by a succession of three binary collisions when three nucleons are in the collision distance with each other at the initial stage. The Pauli principle is respected only at the final states, $\mathbf{P}_1'$, $\mathbf{P}_2'$, $\mathbf{P}_3'$, but not at the intermediate states, $\mathbf{a}$, $\mathbf{b}$, $\mathbf{c}$. The 3*N*C probability increases as the density increases, as pointed out in Ref. [31], and therefore it occurs mostly at the early stage of the reaction before the generated hot-high density nuclear matter expands. As demonstrated in Refs. [9,14], the 3*N*C term enhances the high-energy nucleon production. This is simply because in

3*N*C, the kinetic energy of the three nucleons can be shared among them. This makes a significant difference in the high-energy proton energy spectra between the simulations with turning on and off the 3*N*C process, which is demonstrated in Ref. [9]. Therefore, the high-energy nucleon emission mechanism in the 3*N*C term is purely kinematic effect in the code. This modified version of AMD is called AMD/D-3NC.

These two processes become effective at different incident energy regions. Fermi boost becomes important for the high-energy nucleon production in the heavy-ion reactions below 50 MeV/nucleon, and the 3*N*C process becomes effective in those around 100 MeV/nucleon and above. For cluster productions and their studies, AMD/D works very well. Note that all of the AMD versions described in this article are far from perfect yet and each has good and poor parts. Therefore a proper version should be applied according to the reaction studies and the reaction systems at a given incident energy.

C. Semirelativistic antisymmetrized molecular dynamics

At the incident energies, $E_{\rm inc}/A \geqslant 100$ MeV, the relativistic effect becomes non-negligible. In the original, AMD simulations are performed, using the nonrelativistic Hamiltonian, given in Eq. (7). In the present work we keep this nonrelativistic formulation, following Ref. [32]. There are two crucial parameters whose values may cause noticeably changes in the neutron energy spectra in the laboratory frame between nonrelativistic and relativistic treatments. One is the center of mass (CM) momentum and the other is the neutron kinetic-energy calculation. The center of mass (CM) momentum increases as shown in Fig. 2(a) for the relativistic calculation. After the nonrelativistic simulations are performed according to the formulation presented in Sec. II A, the neutron kinetic energies are calculated in the relativistic and nonrelativistic forms and presented in Fig. 2(b) for AMD/D and AMD/D-3NC. In each case the relativistic calculation of the neutron kinetic energy is reduced about 20% at $E_{\rm kin} \geqslant 200$ MeV compared with those from the nonrelativistic calculation.

For AMD/D, the high-energy neutron yields exponentially falloff more rapidly above 200 MeV. This indicates that the high-energy neutron productions are dominated by the incorporated stochastic processes, especially by the 3*N*C process, and they are independent of the nonrelativistic or relativistic formulation except for the total-energy conservation after the process is performed. The total-energy restoration is performed by making slight shifts in phase space of those among the surrounding nucleons and rather insensitive to the high-energy neutron production. Therefore in the following scenario for the relativistic treatment, the nonrelativistic form is kept in the AMD simulations and the relativistic corrections are performed for these simulated results.

In the original AMD in Ref. [20] simulations are performed nonrelativistically in the CM frame. To compare the neutron energy spectra and angular distributions with the experimental data, the simulated results have to be transformed into the laboratory (LAB) frame. The relativistic corrections are made in three steps. At the beginning of the calculation (front end), the input system is boosted from the LAB frame to the CM frame. At the end of the simulation (back end), the same boost, but with opposite sign, is applied. Since the CM momentum boost becomes larger for the relativistic treatment as shown in Fig. 2(a), the relativistic transformation at the front end reduces the neutron energy and that at the back end enhances the neutron energy. At the back end, the relativistic form is also used to calculate the neutron energy as presented in Fig. 2(b), which results in significant reduction of the neutron energy. Each correction makes significant effects on the neutron energy spectra.

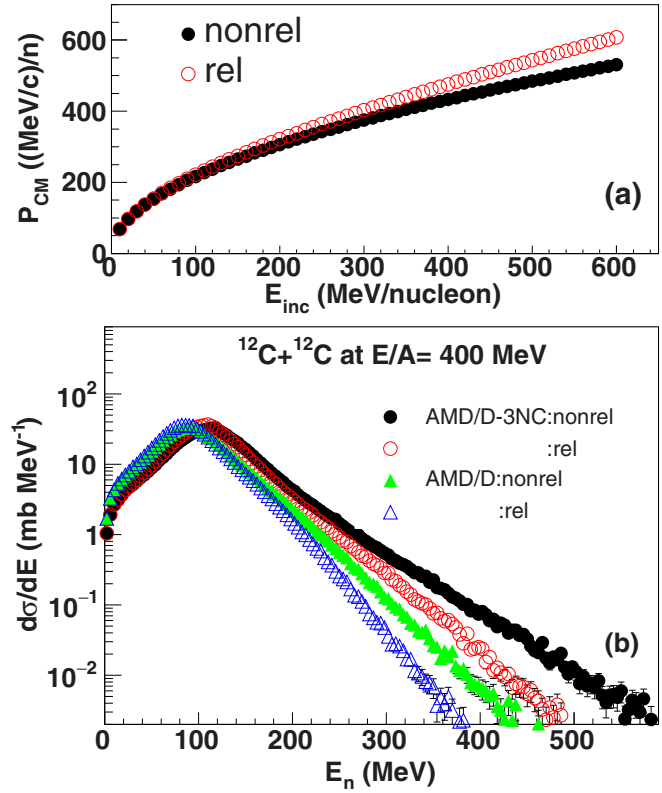

FIG. 2. Nonrelativistic and relativistic energy calculations are compared for (a) the CM momentum and (b) neutron kinetic energy in the CM frame for $^{12}C + ^{12}C$ at 400 MeV/nucleon.

To demonstrate the effect at each correction, the changes of the energy spectra are presented in Fig. 3 with the relativistic correction at the front end alone, with the two corrections at the back end alone and with all three corrections separately, using AMD/D-3NC calculations for $^{12}C + ^{12}C$ at 400 MeV/nucleon. The original nonrelativistic neutron energy spectra are shown by blue histograms. Those with corrections at the front end alone and at the back end alone are shown by light blue and green histograms, respectively. At forward angles, large deviations from the nonrelativistic spectra are made in both corrections and the deviations are slightly larger at the back end. At larger angles both deviations become smaller, especially at the front end.

Since the corrections tend to compensate each other, the final energy spectra both with front and back end corrections become similar to those of the nonrelativistic ones as presented by the red histograms. There are some noticeable differences observed at forward angles, but they are rather

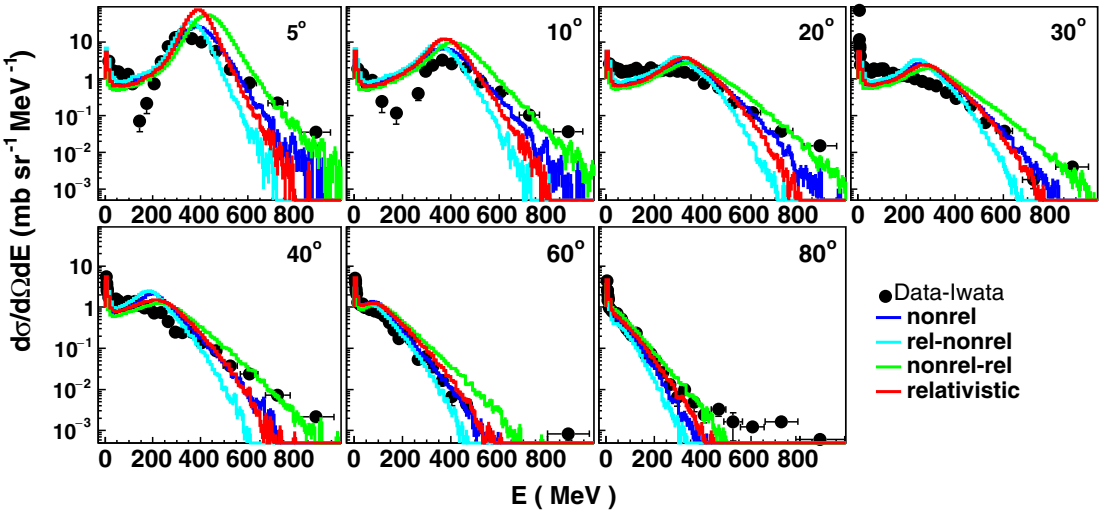

FIG. 3. The three steps of the relativistic treatments are presented separately for AMD/D-3NC simulations for $^{12}C + ^{12}C$ at 400 MeV/nucleon. Blue, light blue, green, and red histograms represent the results of nonrelativistic, the front end alone (denoted rel-nonrel), the back end alone (nonrel-rel) and all three steps corrections (relativistic), respectively. The data are taken from Iwata's data set in Refs. [18,33].

marginal. In the following analysis, these three-step corrections are made for the nonrelativistic AMD calculations and the simulated results are denoted semirelativistic AMD (SR-AMD). The relativistic treatment taken in this work is semirelativistic, since the corrections are made for the kinematics of the nonrelativistic simulated events, and nucleon-nucleon inelastic and meson production processes are not taken into account.

A similar application of the nonrelativistic AMD is made in Ref. [32] for the theoretical study of the nuclear symmetry energy for the pion production in $^{132}Sn + ^{124}Sn$ at 300 MeV/nucleon. In their study, AMD is combined with JAM, a relativistic transport model, in which the former treats the time evolution of the wave packets in the mean field and the latter is used for the meson production, especially for pions. The kinematic connection between these two models are made within the relativistic formulation, but the nonrelativistic Hamiltonian in Eq. (7) is used in the AMD simulation part [34].

III. SIMULATIONS AND RESULTS

The semirelativistic AMD simulations are applied to reproduce the available experimental data to study the production mechanisms of the high-energy neutrons.

In experiments, precise measurements of neutron production double-differential cross sections are a big challenge, especially for those with energy above 100 MeV/nucleon. Among the available experimental data sets, as mentioned in the introduction, we utilized the data sets of $^{12}C + ^{12}C$ at 290 and 400 MeV/nucleon and $^{16}O + ^{12}C$ at 290 MeV/nucleon [18,19] in this study. The data set in Ref. [18] is referred as Iwata's data and those in Ref. [19] as Satoh's data below. Neutrons with energies up to about 900 MeV, were measured by the time-of-flight method. In both experiments, the experimental setups were very similar to each other. The experimental data are combined if they are available in both experiments. Their measured angles were slightly different for the reaction systems between $\theta_{lab} = 5^\circ$ and 90°.

AMD/D-FM and AMD/D-3NC are applied for these reactions with a standard Gogny effective interaction and a constant 3*N*C cross section of 40 mb, which corresponds to the hard-core nucleon-nucleon scattering and is same as that in Refs. [7,30]. In Ref. [30], the three-body cross section $N3$ is given as

$$N3 = \frac{16}{3\pi}\sigma^{5/2}\rho^3\sqrt{T/m}V, \tag{14}$$

where σ is the nucleon-nucleon cross section, ρ is the density, T is the temperature, m is the nucleon mass, and V is the system volume. One should note that $N3$ in Eq. (14) is evaluated for a uniform nuclear matter. In the AMD simulations, when three nucleons meet within a collision distance, the surrounding density and temperature together with the front factor are dynamically simulated in the time evolution of the wave packets. Therefore, the actual 3*N* collision cross section, σ_{3N}, used in the code is simply given by $\sigma_{3N} = \sigma^{5/2}$. About one to two million events are simulated for each case in the impact-parameter range of $b = 0 - 8$ fm. For $b > 8$ fm very few collisions are observed. The semirelativistic corrections are made for all AMD/D-FM and AMD/D-3NC simulated results and they are denoted SR-AMD-FM and SR-AMD-3NC, respectively.

In Fig. 4, the simulated and experimental results for the $^{12}C + ^{12}C$ reaction at 290 MeV/nucleon are compared over the observed angles. All results are plotted in an absolute scale. The high-energy neutrons at larger angles are reasonably well reproduced both by AMD/D-3NC and SR-AMD-3NC, especially for those from Iwata's data, whereas SR-AMD-FM predicts much softer high-energy tails at these angles. Satoh's data well agree with those of Iwata's data at 30° where both measurements were made at the same angle, whereas at 75° and 90°, Satoh's data show about twice larger cross

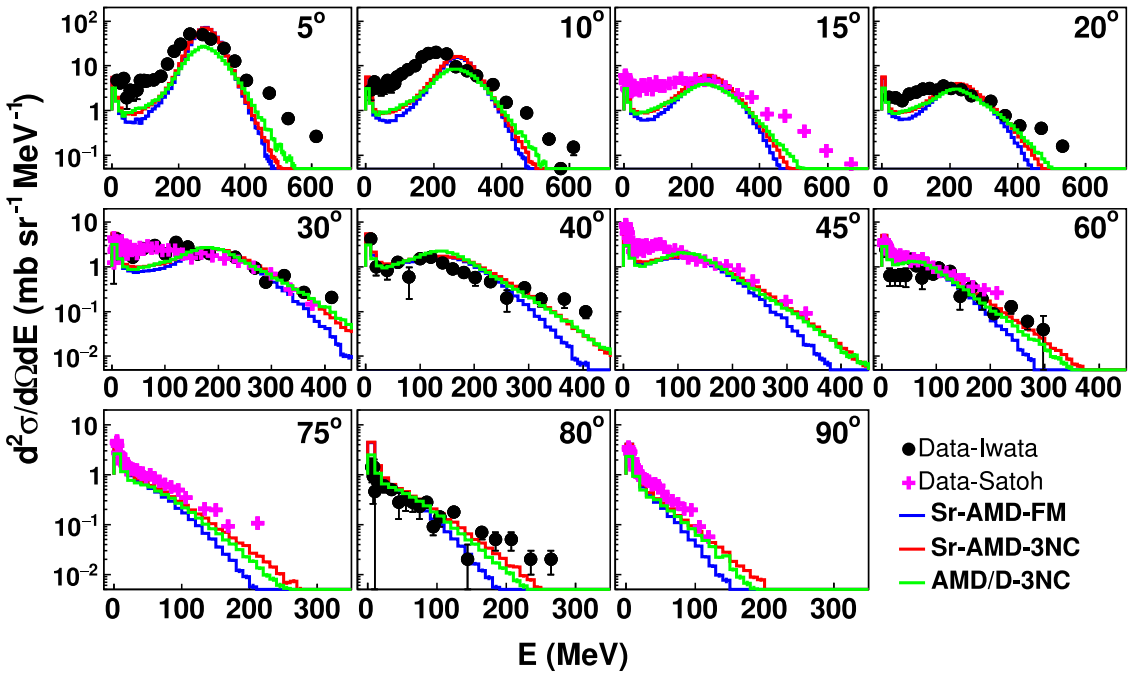

FIG. 4. Neutron double-differential cross sections for $^{12}C + ^{12}C$ collisions at 290 MeV/nucleon. Black solid circles and purple crosses are the experimental data taken from Refs. [18,33] and Ref. [19], respectively. Blue, red, and green histograms are calculated with SR-AMD-FM, SR-AMD-3NC, and AMD/D-3NC, respectively.

sections than those of the calculations. On the other hand, the double-differential cross sections at 80° from Iwata's data are well reproduced by both AMD/D-FM and AMD/D-3NC at low energies, and indeed these cross sections are smaller by a factor of about two compared with those of Satoh's data at 75° and 90°. Therefore, the origin of the discrepancies between the experimental data and the simulations at 75° and 90° are inconclusive for its origins either from the experiments or from the AMD simulations. The neutron spectra from Iwata's data at 40°, 60°, and 80° are reasonably well reproduced with the 3*N*C process in the entire energy range. At 5° the peak yield is better reproduced by SR-AMD, but the experimental peak energy is slightly low and its width is slightly wider. The experimental yields on the low-energy side at $\theta \leqslant 30°$ are significantly larger than those of all simulations. In Fig. 5, the simulated neutron spectra are plotted with the experimental $^{12}C + ^{12}C$ reaction at 400 MeV/nucleon from $\theta_{lab} = 5°$ to 80°. The high-energy neutrons at $\theta \geqslant 60°$ are rather well

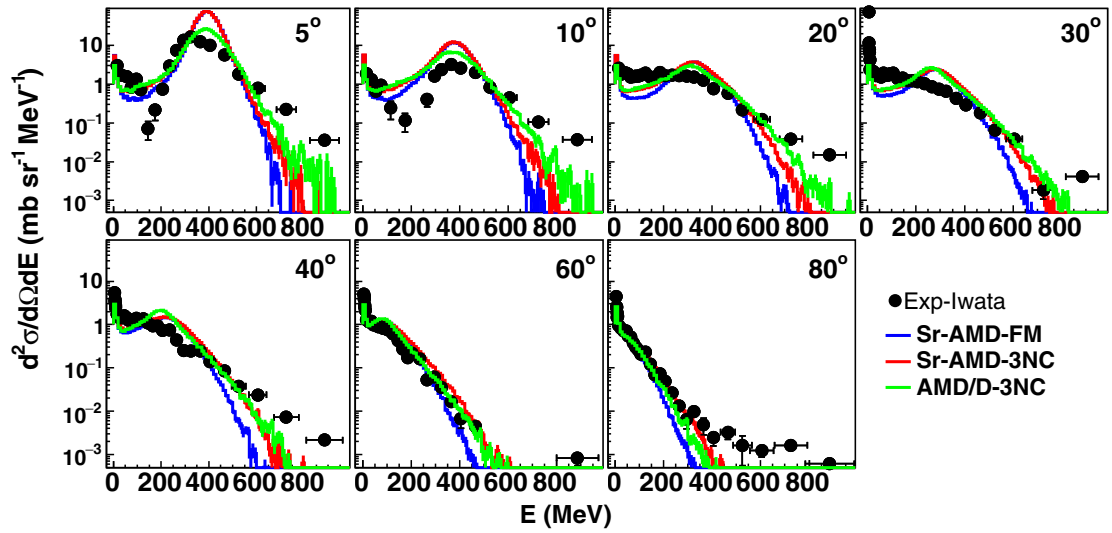

FIG. 5. Neutron double-differential cross sections for $^{12}C + ^{12}C$ collisions at 400 MeV/nucleon. Black solid circle points are experimental data taken from Ref. [18]. Histograms are same as those in Fig. 4.

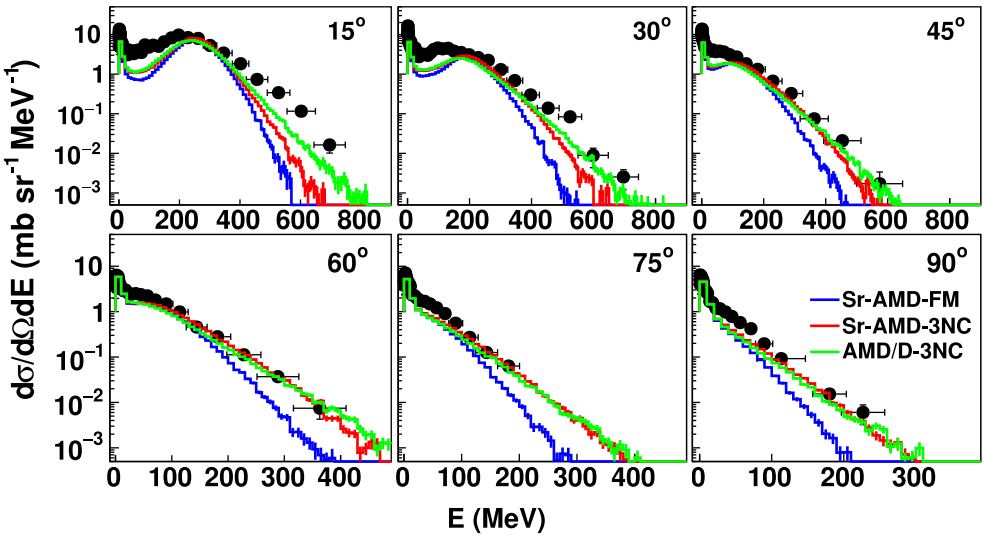

FIG. 6. Neutron double-differential cross sections of $^{16}O + ^{12}C$ collisions at 290 MeV/nucleon. Black solid circles are the experimental data taken from Ref. [19]. Blue, red, and green histograms are same as those in Fig. 4.

reproduced both with AMD/D-3NC and SR-AMD-3NC, whereas SR-AMD-FM predicts slightly softer high energy tails at these angles. On the low-energy side, significant overpredictions are observed. At $\theta = 5^\circ$ and 10° all AMD simulations overpredict the yields but at $20^\circ \leqslant \theta \leqslant 40^\circ$ they underpredict the yields. At angles $\theta \leqslant 40^\circ$, all AMD simulations show a pronounced quasi-elastic peak with about twice larger cross sections. This feature is quite in contrast with the experimental results, especially at $20^\circ \leqslant \theta \leqslant 40^\circ$. The experimental data do not show any peak structure but show a rather broad shoulder. This may cause the significant underpredictions on the lower-energy side. On the contrary, at $\theta = 5^\circ$ and 10°, the experimental data show peaks with similar widths, but two to three times less yield. These discrepancy patterns are quite different from those in Fig. 4. The different discrepancy patterns in peak position and amplitude between the simulations and the experimental results at these forward angles may suggest that they are caused by the experiments.

The semirelativistic and nonrelativistic AMD models are also applied to $^{16}O + ^{12}C$ at 290 MeV/nucleon and the results are shown in Fig. 6. The experimental high-energy neutron tails are well reproduced in overall with the 3*N*C process in this case, except at $\theta = 15^\circ$. At $\theta = 15^\circ$ the experimental tail is harder than the nonrelativistic one. SR-AMD-FM again predicts significantly softer tails than the experimental ones. At angles $\theta \leqslant 45^\circ$, the experimental low-energy yields are significantly underpredicted by about a factor of two for all three simulations.

For the above three reaction systems, nonrelativistic AMD (green histograms) and SR-AMD (red) both with 3*N*C resemble each other, especially at larger angles. A missing relativistic treatment in SR-AMD is the time evolution of the wave packet in the effective mean field. As discussed in Sec. II C, it is expected that the relativistic time evolution will not change the neutron spectra so much, since this does not affect low-energy neutrons, and high-energy neutrons are mostly generated by the incorporated stochastic processes. Therefore, the above results indicate that the nonrelativistic AMD is still valid in the incident energy range studied here.

However, the similarity between the nonrelativistic and semirelativistic results obtained in this study is not guaranteed at higher incident energies nor in other heavier reaction systems. We actually observed noticeable effects of the semirelativistic treatments in the data analysis of the incident energies 560–600 MeV/nucleon at large angles, but these results will be presented in our future works.

IV. SUMMARY

AMD/D-FM and AMD/D-3NC are applied for the high-energy neutron productions in light heavy-ion collisions, using the $^{12}C + ^{12}C$ and $^{16}O + ^{12}C$ reactions at 290 and 400 MeV/nucleon. The relativistic corrections are made to the nonrelativistic AMD simulations to apply them to the experimental data at these incident energies. The semirelativistic versions of AMD/D-3NC and AMD/D-FM are applied to the above experimental data, as well as the original nonrelativistic versions. The final semirelativistic results end up similar to the original nonrelativistic results. For all cases, the high-energy neutron tails are well reproduced by AMD with 3*N*C. AMD/D-FM simulations significantly underpredict these high-energy neutron productions. These observations, therefore, suggest that the high-energy neutrons with energy above the incident-beam energy per nucleon are mainly produced by the 3*N*C process. Overall, these results are consistent to the results obtained around $E_{\rm inc}/A \approx 100$ MeV. On the other hand, all simulations fail to reproduce the low-energy neutrons below the beam energy at angles around $20^\circ - 45^\circ$, although the reason for the discrepancies below 15° are left inconclusive either from the experiments or from the simulations. To confirm our results of the 3*N*C process in the energetic nucleon emissions, further precise experiments are necessary in the future. The High Intensity heavy-ion Accelerator Facility (HIAF) [35], which is being built in China, as well as other facilities such as FRIB and RIKEN, will provide the opportunity to probe the

emission mechanism of high-energy nucleons and subthreshold particles.

ACKNOWLEDGMENTS

We would like to thank Prof. A. Ono for providing the AMD/D source codes and Dr. Y. Iwata for providing their numerical data sets of the experimental cross sections for all reaction systems. We also thank Dr. N. Ikeno for her helpful comments about their work. We acknowledge Dr. Hao Qiu for reviewing the paper. We also thank Dr. J. Z. Duan for help with computing. This work was supported by the Strategic Priority Research of Chinese Academy of Sciences, Grant No. XD34030000, the National Natural Science Foundation of China under Grant No. U1832205, and the US Department of Energy under Grant No. DE-FG02-93ER40773.

[1] G. F. Bertsch and S. Das Gupta, A guide to microscopic models for intermediate energy heavy ion collisions, Phys. Rep. **160**, 189 (1988).
[2] W. Cassing, V. Metag, U. Mosel, and K. Niita, Production of energetic particles in heavy-ion collisions, Phys. Rep. **188**, 363 (1990).
[3] C. K. Gelbke, Space-time information from two-particle correlations, Prog. Part. Nucl. Phys. **42**, 91 (1999).
[4] P. Sapienza, R. Coniglione, M. Colonna *et al.*, Strong enhancement of extremely energetic proton production in central heavy ion collisions at intermediate energy, Phys. Rev. Lett. **87**, 072701 (2001).
[5] B. Friedman and V. R. Pandharipande, Hot and cold, nuclear and neutron matter, Nucl. Phys. A **361**, 502 (1981).
[6] J. Fujita and H. Miyazawa, Pion theory of the three-body forces, Prog. Theor. Phys. **17**, 360 (1957).
[7] A. Bonasera, F. Gulminelli, and J. Molitpris, The Boltzmann equation at the borderline, Phys. Rep. **243**, 1 (1994).
[8] A. Bohnet, N. Ohtsuka, J. Aichelin, R. Linden, and A. Faessler, Quantum molecular-dynamics approach to heavy-ion collisions with Brueckner *g*-matrix cross sections, Nucl. Phys. A **494**, 349 (1989).
[9] R. Wada, Three-nucleon interaction in heavy-ion collisions at intermediate energies, Phys. Rev. C **96**, 031601(R) (2017).
[10] E. Migneco, C. Agodi, R. Alba *et al.*, MEDEA: A multi element detector array for gamma ray and light charged particle detection at the LNS-Catania, Nucl. Instrum. Methods Phys. Res., Sect. A **314**, 31 (1992).
[11] J. Julien, D. Lebrun, A. Mougeot *et al.*, Subthreshold k^+ production in heavy ion collisions, Phys. Lett. B **264**, 269 (1991).
[12] R. Legrain, J. F. Lecolley, F. R. Lecolley *et al.*, Kaon production in nucleus-nucleus collisions at 92 MeV per nucleon, Phys. Rev. C **59**, 1464 (1999).
[13] F. R. Lecolley, N. Alamanos, L. Bianchi *et al.*, Kaon production in nucleus-nucleus collisions at 92 MeV per nucleon, Nucl. Phys. A **583**, 379 (1995).
[14] M. Germain, P. Eudes, F. Guilbault *et al.*, High transverse momentum proton emission in Ar + Ta collisions at 94 MeV/u, Nucl. Phys. A **620**, 81 (1997).
[15] P. Sapienza, R. Coniglione, E. Migneco *et al.*, Hard photon and energetic proton emission in heavy ion collisions at intermediate energy, Nucl. Phys. A **630**, 215 (1998).
[16] P. Sapienza, R. Coniglione, M. Colonna *et al.*, Energetic particle emission and nuclear dynamics around the fermj energy, Nucl. Phys. A **734**, 601 (2004).
[17] R. Coniglione, P. Sapienza, E. Migneco *et al.*, High energy proton emission in heavy ion reactions close to the Fermi energy, Phys. Lett. B **471**, 339 (2000).
[18] Y. Iwata, T. Murakami, H. Sato *et al.*, Double-differential cross sections for the neutron production from heavy-ion reactions at energies $E/A = 290$–600 MeV, Phys. Rev. C **64**, 054609 (2001).
[19] D. Satoh, D. Moriguchi, T. Kajimoto *et al.*, Measurement of neutron-production double-differential cross-sections on carbon bombarded with 290-MeV/nucleon carbon and oxygen ions, Nucl. Instrum. Methods Phys. Res., Sect. A **644**, 59 (2011).
[20] A. Ono, H. Horiuchi, T. Maruyama *et al.*, Antisymmetrized version of molecular dynamics with two-nucleon collisions and its application to heavy ion reactions, Prog. Theor. Phys. **87**, 1185 (1992).
[21] J. Dechargé and D. Gogny, Hartree-Fock-Bogolyubov calculations with the $D1$ effective interaction on spherical nuclei, Phys. Rev. C **21**, 1568 (1980).
[22] G. Q. Li and R. Machleidt, Microscopic calculation of in-medium nucleon-nucleon cross sections, Phys. Rev. C **48**, 1702 (1993).
[23] G. Q. Li and R. Machleidt, Microscopic calculation of in-medium proton-proton cross sections, Phys. Rev. C **49**, 566 (1994).
[24] A. Ono, Dynamics of clusters and fragments in heavy-ion collisions, Prog. Part. Nucl. Phys. **105**, 139 (2019).
[25] R. Han, Z. Chen, and R. Wada, A. Ono, G. Tian, F. Shi, X. Zhang, B. Liu, and H. Sun, Effects of cluster correlations on fragment emission in $^{12}C + ^{12}C$ at 50 MeV/nucleon, Phys. Rev. C **102**, 064617 (2020).
[26] W. Lin, X. Liu, R. Wada *et al.*, High-energy proton emission and Fermi motion in intermediate-energy heavy-ion collisions, Phys. Rev. C **94**, 064609 (2016).
[27] A. Ono and H. Horiuchi, Antisymmetrized molecular dynamics of wave packets with stochastic incorporation of the Vlasov equation, Phys. Rev. C **53**, 2958 (1996).
[28] A. Ono, Antisymmetrized molecular dynamics with quantum branching processes for collisions of heavy nuclei, Phys. Rev. C **59**, 853 (1999).
[29] A. Ono and H. Horiuchi, Improvement of the nucleon emission process and the statistical property in molecular dynamics, Phys. Rev. C **53**, 845 (1996).
[30] A. Bonasera and F. Gulminelli, Competition between two- and three-body collisions in a dense gas at finite, Phys. Lett. B **259**, 399 (1991).
[31] St. Mrówczyński, Applicability of transport theory of gases to the description of excited nuclear matter, Phys. Rev. C **32**, 1784 (1985).
[32] N. Ikeno, A. Ono, Y. Nara, and A. Ohnishi, Probing neutron-proton dynamics by pions, Phys. Rev. C **93**, 044612 (2016).

[33] Y. Iwata (private communication). The plotted data are from the numerical data set, which were kindly sent to us by Dr. Y. Iwata (2023).
[34] N. Ikeno (private communication, 2023).
[35] J. C. Yang, J. W. Xia, and G. Q. Xiao *et al.*, High intensity heavy ion accelerator facility (HIAF) in China, Nucl. Instrum. Methods Phys. Res., Sect. B **317**, 263 (2013).